Electric Power Systems Research 262 (2027) 113547

Contents lists available at ScienceDirect

Electric Power Systems Research

journal homepage: www.elsevier.com/locate/epsr

Dynamic phasor state-space solver for hybrid AC/DC systems

Saif Alsarayreh *, Robert Dimitrovski, Aleksandra Lekić

Electrical Sustainable Energy, Delft University of Technology, Delft, The Netherlands

ARTICLE INFO

Keywords:
Dynamic phasors
DQsym framework
HVDC transmission
Modular-multilevel converter (MMC)

ABSTRACT

This paper presents a dynamic phasor-based state-space modelling framework for modular multilevel converters (MMCs) using multiple dq reference frames ($DQsym$). The main contribution is the development of a numerically stable state-space solver tailored to multi-dq dynamic phasor models. The solver employs integration and a systematic matrix update mechanism to consistently incorporate switching events within the unified state-space formulation, allowing harmonic interactions and topology changes to be captured without manual reconfiguration. The proposed framework is implemented as a standalone MATLAB/Simulink library to facilitate time-domain simulation and to provide a structured basis for future eigenvalue-based small-signal stability studies. The approach is validated on a point-to-point HVDC system and benchmarked against an EMT model. Results demonstrate that the $DQsym$-based implementation achieves EMT-level fidelity while maintaining state-space structure suitable for scalable, system-level analysis of converter-dominated grids.

1. Introduction

The modular multilevel converter (MMC) is widely used in high-voltage direct current (HVDC) transmission and grid-support applications because it is scalable and built from repeatable submodules. However, its internal behaviour is complex. The capacitor voltages, circulating currents, and harmonic components inside the converter introduce time-varying effects that make accurate system-level modelling difficult [1–3]. These challenges become more significant in converter-dominated grids, where several MMC stations interact with each other and with network resonances. In such cases, both fundamental-frequency and harmonic dynamics must be captured.

Electromagnetic transient (EMT) simulations can represent these effects with high accuracy, but they are computationally demanding for large networks and often time-consuming for stability studies. In contrast, average-value and dq-frame models are computationally efficient, but they usually neglect important harmonic interactions, which can reduce accuracy when harmonics strongly influence system behaviour [4,5].

Dynamic phasor (DP) theory represents time-varying signals using selected Fourier coefficients, leading to time-invariant state-space models that retain both fundamental and key harmonic components [5–7]. This provides a practical balance between detailed switching models and simplified average models. Although DP-based methods have been reported in the literature [8–10], their use in system-level studies remains limited. Many existing implementations are script-based or not structured for modular interconnection, which makes it difficult to build larger and reproducible models, particularly in widely used environments such as MATLAB/Simulink.

Open-source tools such as DPsim [11] offer EMT and dynamic phasor simulation capabilities, mainly for real-time and co-simulation applications. However, these tools are primarily code-oriented and do not provide block-based libraries that can be directly integrated into MATLAB/Simulink for system-level model development.

The recently proposed $DQsym$ framework in [12] extends DP theory by systematically accounting for harmonic interactions across multiple dq reference frames. Initial validation of a MATLAB/Simulink-based $DQsym$ library on a single MMC station showed accuracy comparable to EMT simulations, highlighting its potential as a practical modelling approach.

To enable broader application, $DQsym$ must be integrated into a solver capable of handling switching events and more complex network configurations. Applications such as point-to-point and multi-terminal HVDC systems require accurate harmonic representation for reliable time-domain and future stability studies [13,14]. Embedding the $DQsym$ formulation into a discrete state-space solver provides an efficient and accurate framework for analysing converter-dominated grids.

This paper advances the $DQsym$ approach in two key aspects. First, the formulation is embedded within a unified state-space solver that systematically handles switching events through matrix updates while preserving harmonic state continuity and numerical stability. Second, although validation is performed on a two-terminal HVDC link, the

* Corresponding author.
E-mail addresses: S.T.S.Alsarayreh@tudelft.nl (S. Alsarayreh), R.Dimitrovski@tudelft.nl (R. Dimitrovski), A.Lekic@tudelft.nl (A. Lekić).

https://doi.org/10.1016/j.epsr.2026.113547
Received 13 October 2025; Received in revised form 3 March 2026; Accepted 20 June 2026
Available online 27 June 2026

proposed framework is modular and converter-oriented, without relying on point-to-point topology assumptions. The formulation can therefore be extended directly to multi-terminal HVDC systems. Future work will focus on validation in large-scale DC grids to further assess scalability.

The main contributions of this paper are summarized as follows:

- Formulation of a unified state-space solver for multi-dq dynamic phasor models of MMCs, enabling consistent simulation.
- Development of an integrated matrix update mechanism that incorporates switching actions directly into the state-space framework.
- Implementation and validation of the proposed approach on a point-to-point HVDC system, benchmarked against an EMT model to assess accuracy.

The remainder of this paper is organized as follows. Section 2 introduces the fundamentals of dynamic phasor theory and details the proposed $DQsym$ formulation. Section 3 introduce the state-space solver algorithm. Section 4 presents the operating principles of the MMC and develops a nonlinear averaged model in $DQsym$. Section 5 reports simulation results of a point-to-point HVDC system benchmarked against EMT. Finally, Section 6 concludes the paper and outlines future research directions.

2. Dynamic phasor theory and DQsym

2.1. Dynamic phasors

Dynamic phasors (DPs) express signals as time-varying Fourier coefficients, capturing both fundamental and harmonic dynamics in a compact framework [15]. For a nearly periodic signal $x(\tau)$, the k^{th} dynamic phasor is defined as $\langle x\rangle_k(t)$, with $\omega_c = 2\pi/T$. The original signal $x(t)$ can be reconstructed by remodulation and taking the real part:

- $\langle x\rangle_k(t) = \frac{1}{T}\int_{t-T}^{t} x(\tau)e^{-jk\omega_c\tau}\,d\tau$,
- $x(t) = \Re\left\{\sum_{k=-K}^{K}\langle x\rangle_k(t)e^{jk\omega_c t}\right\}$

DPs inherit several useful properties from the Fourier series, making them well-suited for modeling systems with harmonic coupling. The number of retained harmonics k determines the trade-off between model fidelity and computational cost. Their key properties include:

- **Time derivative:** $\frac{d\langle x\rangle_k}{dt} = \left\langle \frac{dx}{dt}\right\rangle_k - jk\omega_c\langle x\rangle_k$,
- **Multiplication:** $\langle xy\rangle_k = \sum_i \langle x\rangle_{k-i}\langle y\rangle_i$,
- **Conjugate symmetry:** $\langle x\rangle_{-k} = \langle x\rangle_k^*$.

2.2. $DQsym$ approach

$DQsym$ framework extends dynamic phasor (DP) representations to the dq domain with multiple $dq0$ frames, facilitating the modelling of signals with harmonics within a well-established state-space structure.

Following [16], the procedure for the transformation of DP quantities from the abc frame into the $dq0$ frame, consists of: (i) employing the symmetrical component transformation T_{pnz} to decompose three-phase signals into positive-, negative-, and zero-sequence components, and which is equal to DPs in $\alpha\beta$ frame (ii) rotating the positive and negative sequences into the $dq0$ frame via the Park transformation. This results in the compact relation

$$\begin{bmatrix}\langle x_{dq,p}\rangle_k\\ \langle x_{dq,n}\rangle_k\\ \langle x_{dq,z}\rangle_k\end{bmatrix} = \begin{bmatrix}\mathbf{x}_d^p(k)+j\mathbf{x}_q^p(k)\\ \mathbf{x}_d^n(k)+j\mathbf{x}_q^n(k)\\ \mathbf{x}_d^z(k)+j\mathbf{x}_q^z(k)\end{bmatrix}. \tag{1}$$

This formulation maps dynamic phasors in the abc frame to the $dq0$ frame, providing the foundation for the proposed $DQsym$ framework. Full derivations and proofs are provided in [16]. Eq. (2) summarises this transformation: DPs are first constructed in the abc frame using in-phase and quadrature coefficients (C^c and C^s), then transformed into symmetrical components, and finally rotated into the $dq0$ frame.

$$\begin{aligned}&\begin{bmatrix}\mathbf{C}_k^c+j\mathbf{C}_k^s\\ \mathbf{C}_k^c+j\mathbf{C}_k^s\\ \mathbf{C}_k^c+j\mathbf{C}_k^s\end{bmatrix} = \begin{bmatrix}\langle x_a\rangle_k\\ \langle x_b\rangle_k\\ \langle x_c\rangle_k\end{bmatrix} \xRightarrow{T_{pnz}} \begin{bmatrix}\langle x_{\alpha\beta,p}\rangle_k\\ \langle x_{\alpha\beta,n}\rangle_k^*\\ \langle x_{0,z}\rangle_k\end{bmatrix},\\ &\begin{bmatrix}e^{-j\theta}&0&0\\0&e^{-j\theta}&0\\0&0&1\end{bmatrix}\begin{bmatrix}\langle x_{\alpha\beta,p}\rangle_k\\ \langle x_{\alpha\beta,n}\rangle_k^*\\ \langle x_{0,z}\rangle_k\end{bmatrix} \Rightarrow \begin{bmatrix}\langle x_{dq,p}\rangle_k\\ \langle x_{dq,n}\rangle_k\\ \langle x_{dq,z}\rangle_k\end{bmatrix}.\end{aligned} \tag{2}$$

2.3. Mathematical operations

The following set of mathematical operations—summation, multiplication, and integration—form the basis of the DQsym approach and enable its application to full system simulations. In [12], a full derivation and detailed proofs are provided.

Summation: For DP vectors $\mathbf{x}_{dq}^{p,n,z}(k) = \mathbf{x}_d^{p,n,z}(k) + j\,\mathbf{x}_q^{p,n,z}(k)$ and $\mathbf{y}_{dq}^{p,n,z}(k)$, addition is elementwise in the complex domain:

$$\mathbf{z}_{dq}^{p,n,z}(k) = \mathbf{x}_{dq}^{p,n,z}(k) + \mathbf{y}_{dq}^{p,n,z}(k), \quad k \in \{0,1,\dots,n\}. \tag{3}$$

Multiplication: Any T-periodic, nearly periodic, or band-limited signal admits a (truncated) Fourier expansion. Using complex coefficients is most compact to represent such signals:

$$x(t) = \sum_{k=-N}^{N} a_k e^{jk\omega_0 t}, \quad y(t) = \sum_{k=-N}^{N} b_k e^{jk\omega_0 t}, \quad \omega_0 = \frac{2\pi}{T}$$

The product $z(t) = x(t)y(t)$ has coefficients given by the circular convolution which shows that multiplication expands the spectrum to harmonics up to order $2N$. The equivalent real (trigonometric) form,

$$z(t) = C_0 + \sum_{k=1}^{2N}\left(C_k^c\cos k\omega_0 t + C_k^s \sin k\omega_0 t\right), \tag{4}$$

followed by collecting in-phase and quadrature components. Closed-form expressions for C_0, C_k^c, and C_k^s and their correctness by induction are provided in (5). Hence, the multiplication process in $DQsym$ is depicted in Fig. 1 with the following steps:

1) Map $x_{dq}^{p,n,z}$ and $y_{dq}^{p,n,z}$ to phase domain $x_{dq}^{a,b,c}$, $y_{dq}^{a,b,c}$.
2) Extract per-phase Fourier coefficients (sine/cosine or complex).
3) Compute products to obtain C_0, C_k^c, C_k^s (or c_k) up to $2n$ using formulas in (5).
4) Reconstruct $z_{dq}^{a,b,c}$ and transform back to $z_{dq}^{p,n,z}$.

This realizes DP multiplication while preserving the $dq0$ structure and explicitly capturing harmonic growth to order $2n$.

$$\begin{aligned}
C_0 &= a_0 b_0 + \sum_{i=1}^{N}\left(\tfrac{1}{2}a_i^s b_i^s + \tfrac{1}{2}a_i^c b_i^c\right),\\
C_k^s &= \sum_{\substack{i+j=k\\1\le i,j\le N}} \tfrac{1}{2}\left(a_i^s b_j^c + a_i^c b_j^s\right) +\\
&\quad \sum_{\substack{|i-j|=k\\1\le i,j\le N}} \left[\tfrac{1}{2}\left(\operatorname{sgn}(i-j)a_i^s b_j^c - \operatorname{sgn}(i-j)a_i^c b_j^s\right) + a_0 b_k^s + b_0 a_k^s\right]\\
C_k^c &= \sum_{\substack{i+j=k\\1\le i,j\le N}} \tfrac{1}{2}\left(a_i^c b_j^c - a_i^s b_j^s\right) +\\
&\quad \sum_{\substack{|i-j|=k\\1\le i,j\le N}} \left[\tfrac{1}{2}\left(a_i^c b_j^c + a_i^s b_j^s\right) + a_0 b_k^c + b_0 a_k^c\right]
\end{aligned} \tag{5}$$

Integration: Time-varying signals up to the n^{th} harmonic can be expressed by a Fourier series

$$f(t) = a_0 + \sum_{n=1}^{\infty}\left(a_n\cos n\omega_0 t + b_n \sin n\omega_0 t\right). \tag{6}$$

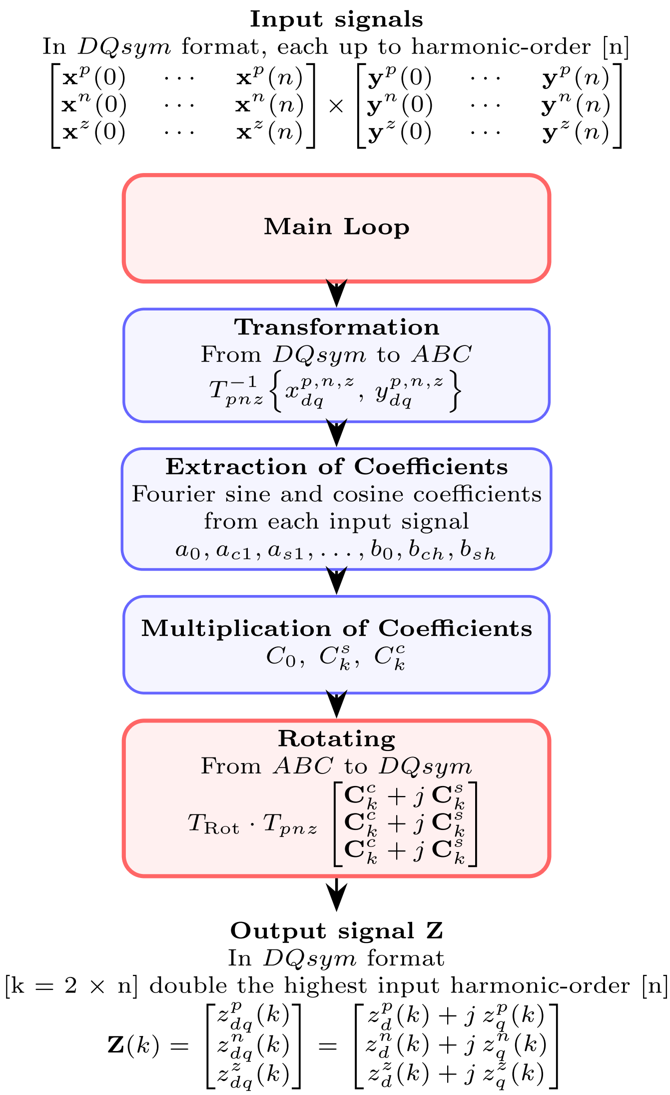

Fig. 1. Flowchart of the multiplication algorithm for harmonic-rich signals $x_{\text{dqn}}^{p,n,z}(i)$ and $y_{\text{dqn}}^{p,n,z}(i)$ [12].

Its antiderivative follows directly from term-by-term integration:

$$F(t) = a_0 t + \sum_{n=1}^{\infty} \frac{a_n}{n\omega_0} \sin n\omega_0 t - \sum_{n=1}^{\infty} \frac{b_n}{n\omega_0} \cos n\omega_0 t. \tag{7}$$

For a complex signal $f_{dq} = f_d(n) + j f_q(n)$, integration yields

$$\int f_{dq}(n) e^{jn\omega_0 t} dt = (f_d + j f_q) \frac{-j}{n\omega_0} e^{jn\omega_0 t} + C, \tag{8}$$

while in the DP representation, where $e^{jn\omega_0 t}$ is removed,

$$\langle F_{dq} \rangle = (f_d + j f_q) \frac{-j}{n\omega_0} + C, \tag{9}$$

highlighting that integration in dq form introduces d-q cross-coupling. This approach extends directly to $\langle f_{dq}^{p,n,z} \rangle$ and $\langle F_{dq}^{p,n,z} \rangle$, preserving vector dimensionality up to the n^{th} harmonic.

3. Dynamic phasor state-space solver

The proposed solver is formulated in the phasor domain using a state-space representation of a switched linear system. The continuous-time model is given by

$$\dot{x}(t) = Ax(t) + Bu(t), \qquad y(t) = Cx(t) + Du(t), \tag{10}$$

where $x \in \mathbb{C}^n$ denotes the state vector, $u \in \mathbb{C}^m$ the input, and $y \in \mathbb{C}^p$ the output. For numerical implementation, the discrete-time matrices (A_d, B_d, C_d, D_d) are obtained from (A, B, C, D) using a standard integration method such as trapezoidal (Tustin) discretisation.

By applying the derivative property of dynamic phasors, the system equations in the DQn domain become

$$\begin{aligned} \dot{x}_k(t) &= \left(A_{dqn} - jk\omega_s I\right) x_k(t) + B_{dqn} u_k(t), \\ y_k(t) &= C_{dqn} x_k(t) + D_{dqn} u_k(t), \end{aligned} \tag{11}$$

where $x_k(t)$ and $u_k(t)$ represent the dynamic phasor states and inputs at harmonic order k, and $y_k(t)$ is the corresponding output.

In power electronic systems, switching devices cause discrete changes in the circuit configuration. These changes must be reflected directly in the state-space matrices. Passive elements remain unchanged over time, but each switch modifies the system equations depending on whether it is on or off. A closed switch is modeled as a low-resistance path with conductance $G_{\text{on}} = 1/R_{\text{on}}$, while an open switch is modeled as a high-resistance path with $G_{\text{off}} = 1/R_{\text{off}}$. These conductances affect the effective matrices (A, B, C, D) and therefore alter the system representation whenever a switching event occurs.

Dynamic phasors describe the system using Fourier components of the states. When switching takes place, the harmonic content changes. Updating the matrices ensures that the harmonic coupling terms (off-diagonal entries in the DP system matrix) are properly adjusted. If switching is not reflected in the matrices, noticeable errors can appear in both transient and steady-state responses.

The state-space framework allows multiple switches to be handled in a consistent manner. Instead of manually redefining system equations for each configuration, the matrices are updated automatically according to the switch vector describing the network state. This approach reduces implementation errors and ensures that switching effects are captured directly through R_{on} and R_{off}. In addition, maintaining the state-space form allows standard eigenvalue-based stability analysis after linearization around an operating point.

To ensure numerical stability when a switching event occurs within a sampling interval, a predictor-corrector scheme is applied [17,18]. Let $(A_d, B_d)_{old}$ denote the matrices before switching, $(A_d, B_d)_{new}$ the updated matrices after switching, and T_s the discretisation time-step. The half-step states are computed as

$$\begin{aligned} x_{T_s-\frac{1}{2}} &= x_{T_s-1} + \tfrac{T_s}{2}\left(\left(A_{\text{old}}^{dqn} - jk\omega_s I\right) x_{T_s-1} + B_{\text{old}}^{dqn} u_{T_s}\right), \\ x_{T_s+\frac{1}{2}} &= x_{T_s-1} + \tfrac{T_s}{2}\left(\left(A_{\text{new}}^{dqn} - jk\omega_s I\right) x_{T_s-1} + B_{\text{new}}^{dqn} u_{T_s}\right), \end{aligned} \tag{12}$$

and the corrected state is obtained as

$$x_{T_s} = \tfrac{1}{2}\left(x_{T_s-\frac{1}{2}} + x_{T_s+\frac{1}{2}}\right). \tag{13}$$

The final state and output updates are then

$$\begin{aligned} x_{T_s+1} &= \left(A_{\text{new}}^{dqn} - jk\omega_s I\right) x_{T_s} + B_{\text{new}}^{dqn} u_k, \\ y_{T_s} &= C_{\text{new}}^{dqn} x_{T_s} + D_{\text{new}}^{dqn} u_{T_s}. \end{aligned} \tag{14}$$

The algorithm shown in Fig. 2 provides an efficient and stable way to simulate switched three-phase systems in the time domain while capturing both transient and steady-state phasor behaviour.

Since the predictor–corrector step is equivalent to applying the trapezoidal rule to a piecewise-constant system matrix during switching, stability follows from the A-stability of the trapezoidal method. For eigenvalues satisfying $\mathrm{Re}(\lambda) \le 0$, the amplification factor

$$\left| \frac{1 + \frac{1}{2} T_s \lambda}{1 - \frac{1}{2} T_s \lambda} \right| \le 1,$$

which guarantees bounded discrete-time solutions. Therefore, the proposed update preserves both accuracy and stability, provided that switching events are properly resolved within the sampling interval.

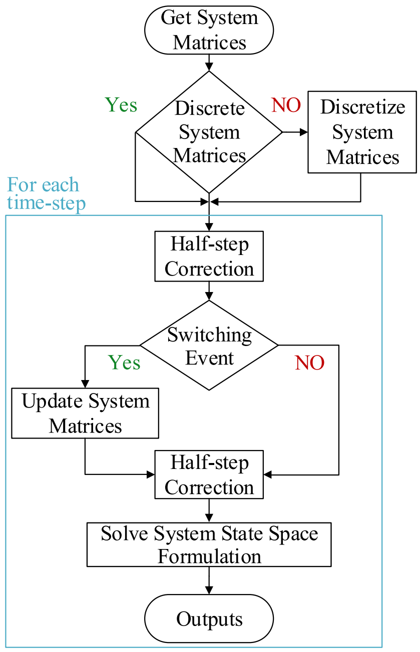

Fig. 2. Flowchart of the state space solver algorithm for harmonic-rich states.

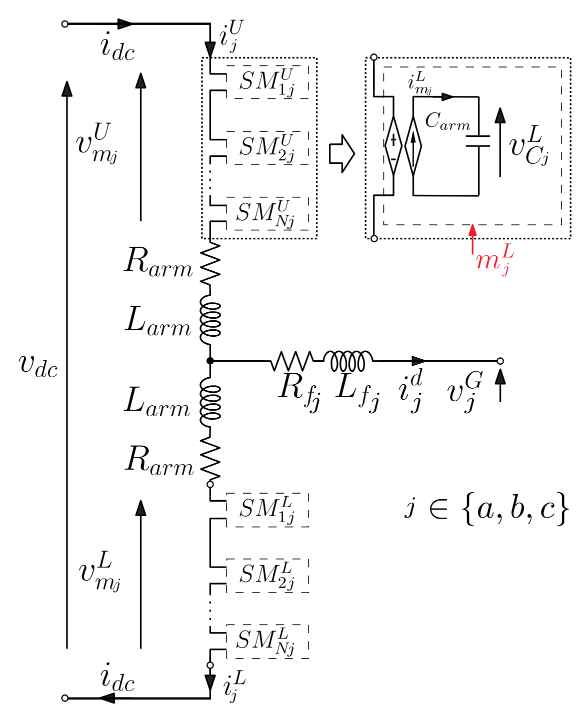

Fig. 3. Circuit diagram of the MMC converter showing the grid current, positive and negative arm current directions.

4. MMC topology and average arm model

The MMC consists of N series-connected submodules (SMs), each with a capacitor C, forming a converter arm. Each arm, comprising an inductor L_{arm} and resistance R_{arm}, is connected between the dc bus and the ac terminal. Two such arms, linked to the upper and lower dc poles, constitute one phase leg $j \in \{a, b, c\}$. The ac-side is interfaced through an equivalent filter impedance $R_f + sL_f$.

Assuming small deviations among SM capacitor voltages, the aggregate behavior of each arm can be captured using the arm average model. In this form, each arm is represented as a controlled voltage source on the ac side, with its dynamic capacitor current ensuring energy balance on the dc side. The resulting equivalent resembles a conventional VSC arm with averaged dynamics. The model adopted here follows the formulation in [19].

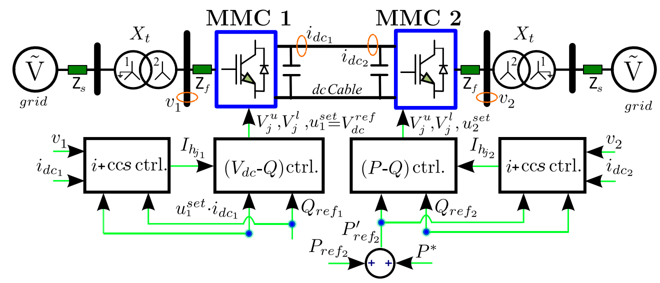

Fig. 4. Point-to-point HVDC transmission system based on two modular multilevel converters (MMC1 and MMC2). Each MMC is equipped with control loops for regulating active/reactive power, DC voltage, and circulating current suppression, while transformer reactances interface the converters with the AC grids [20].

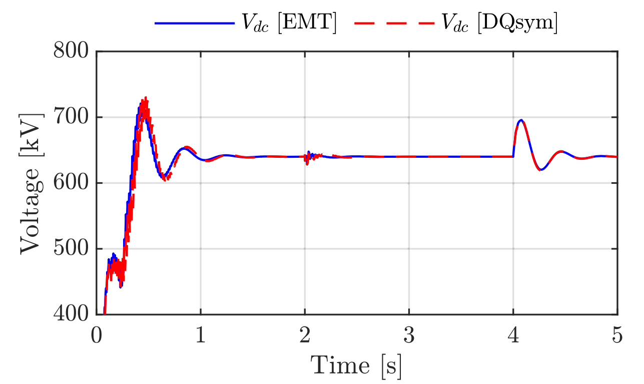

Fig. 5. DC link voltage response of the HVDC MMC system under transient and steady-state conditions, comparing EMT and DQsym simulations.

The outputs of the controlled sources are referred to as the modulated voltages v_{mj}^{u} and v_{mj}^{ℓ} and modulated currents i_{mj}^{u} and i_{mj}^{ℓ} for the upper (^{u}) and lower ($^{\ell}$) arms of a generic phase j. They are described by the following equations:

$$
\begin{aligned}
v_{mj}^{u} &= m_j^{u}\, v_{Cj}^{u}, \qquad & v_{mj}^{\ell} &= m_j^{\ell}\, v_{Cj}^{\ell}, \\
i_{mj}^{u} &= m_j^{u}\, i_j^{u}, \qquad & i_{mj}^{\ell} &= m_j^{\ell}\, i_j^{\ell}.
\end{aligned}
\tag{15}
$$

where v_{Cj}^{u} and v_{Cj}^{ℓ} are the voltages across the upper and lower arm equivalent capacitors. The modulation indices for the upper and lower arms are denoted as m_j^{u} and m_j^{ℓ}, while i_j^{u} and i_j^{ℓ} are the currents in the upper and lower arms, respectively.

To further support the derivation in the following section and to ease the derivation of an MMC representation using the proposed approach, the sum-difference will be used throughout this paper. It is straightforward to redefine the voltages and currents that are defined in Fig. 3 using sum-difference nomenclature as:

$$
\begin{aligned}
i_j^{\Delta} &\triangleq i_j^{u} - i_j^{\ell}, \quad & i_j^{\Sigma} &\triangleq \tfrac{1}{2}\left(i_j^{u} + i_j^{\ell}\right), \\
v_{Cj}^{\Delta} &\triangleq v_{Cj}^{u} - v_{Cj}^{\ell}, \quad & v_{Cj}^{\Sigma} &\triangleq \tfrac{1}{2}\left(v_{Cj}^{u} + v_{Cj}^{\ell}\right).
\end{aligned}
\tag{16}
$$

In this equation, i_j^{Δ} is the current flowing through the ac-side grid, whereas i_j^{Σ} is the well-known circulating current of the MMC. Moreover, v_{Cj}^{Δ} and v_{Cj}^{Σ} represent the difference and the sum of voltages across the upper and lower equivalent capacitors, respectively. It is useful to define the modulation indices in the Σ–Δ representation as

$$
m_j^{\Delta} \triangleq m_j^{u} - m_j^{\ell}, \qquad m_j^{\Sigma} \triangleq m_j^{u} + m_j^{\ell}, \tag{17}
$$

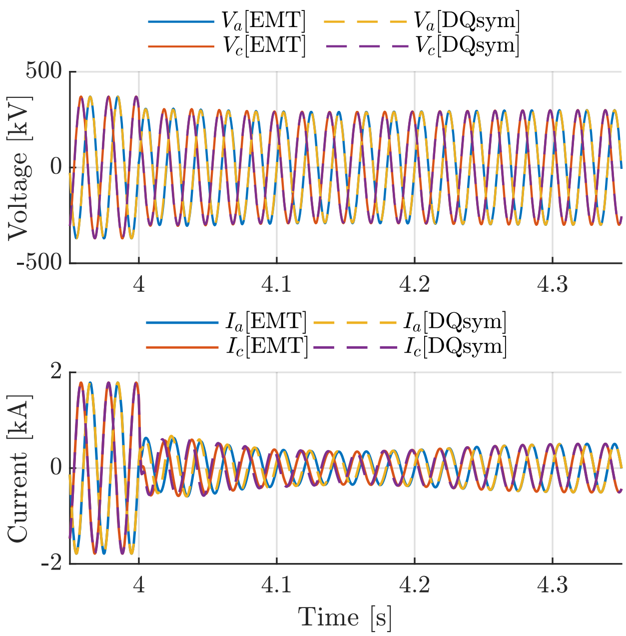

Fig. 6. Comparison of EMT and *DQsym* simulations of inverter-side MMC phase-a and phase-c voltages and currents. A close overlap of waveforms shows that the *DQsym* model accurately reproduces EMT dynamics.

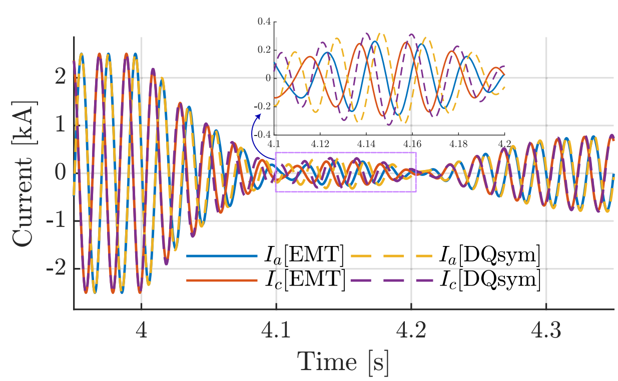

Fig. 7. EMT and *DQsym* simulations of rectifier-side MMC output phase-a and phase-c currents show alignment during transient and steady-state operation.

and the modulated voltages from (15) as

$$v^{\Delta}_{mj} \triangleq -\tfrac{1}{2}\, m^{\Delta}_{j}\, v^{\Sigma}_{Cj} - m^{\Sigma}_{j}\, v^{\Delta}_{Cj},$$
$$v^{\Sigma}_{mj} \triangleq \tfrac{1}{2}\, m^{\Sigma}_{j}\, v^{\Sigma}_{Cj} + m^{\Delta}_{j}\, v^{\Delta}_{Cj}. \tag{18}$$

The three-phase ac-grid currents $\vec{i}^{\Delta}_{j}$ are expressed using vector notation in the stationary frame as

$$L^{ac}_{eq}\frac{d\vec{i}^{\Delta}_{j}}{dt} = \vec{v}^{g}_{j} - R^{ac}_{eq}\,\vec{i}^{\Delta}_{j} - \vec{v}^{\Delta}_{mj}, \tag{19}$$

where $\vec{v}^{g}_{j}$ is the grid voltage vector defined as $\vec{v}^{g}_{j} \triangleq [v^{g}_{a}\ v^{g}_{b}\ v^{g}_{c}]^{T}$, and $\vec{v}^{\Delta}_{mj}$ is the modulated voltage vector driving the ac-grid current is defined as $\vec{v}^{\Delta}_{mj} \triangleq [v^{\Delta}_{ma}\ v^{\Delta}_{mb}\ v^{\Delta}_{mc}]^{T}$. These modulated voltages can be expressed as

$$\vec{v}^{\Delta}_{mj} \triangleq \tfrac{1}{2}\left(\vec{m}^{\Delta}_{j} \odot \vec{v}^{\Sigma}_{C,j} + \vec{m}^{\Sigma}_{j} \odot \vec{v}^{\Delta}_{C,j}\right), \tag{20}$$

where $\odot$ denotes element-wise multiplication of vectors, and $\vec{m}^{\Delta}_{j} \triangleq [m^{\Delta}_{a}\ m^{\Delta}_{b}\ m^{\Delta}_{c}]^{T}$, $\vec{m}^{\Sigma}_{j} \triangleq [m^{\Sigma}_{a}\ m^{\Sigma}_{b}\ m^{\Sigma}_{c}]^{T}$. Furthermore, R^{ac}_{eq} and L^{ac}_{eq} are the equivalent ac resistance and inductance, respectively, are defined as $R_{sum} + \frac{R_{arm}}{2}$ and $L_{sum} + \frac{L_{arm}}{2}$. R_{sum} and L_{sum} are equal to $\frac{R_s+R_t}{k_t^2} + R_f$, $\frac{L_s+L_t}{k_t^2} + L_f$, R_s and L_s are the equivalent internal resistance and inductance of the AC system. R_t and L_t, k_t are the equivalent resistance,

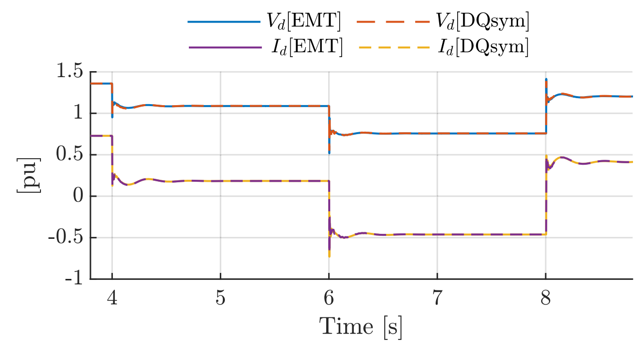

Fig. 8. Direct-axis voltage (V_d) and current (I_d) responses of the inverter-side MMC, comparing EMT and *DQsym* simulations under step changes in reference values.

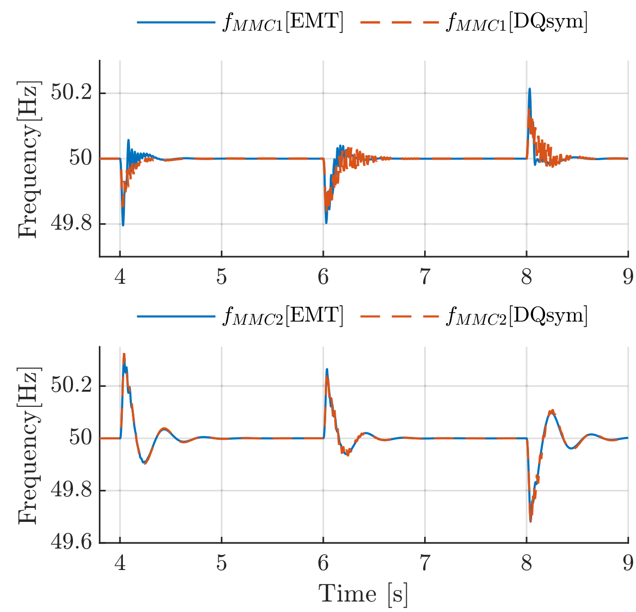

Fig. 9. Comparison of frequency responses of MMC1 (top) and MMC2 (bottom) obtained from EMT and *DQsym* models during transient events.

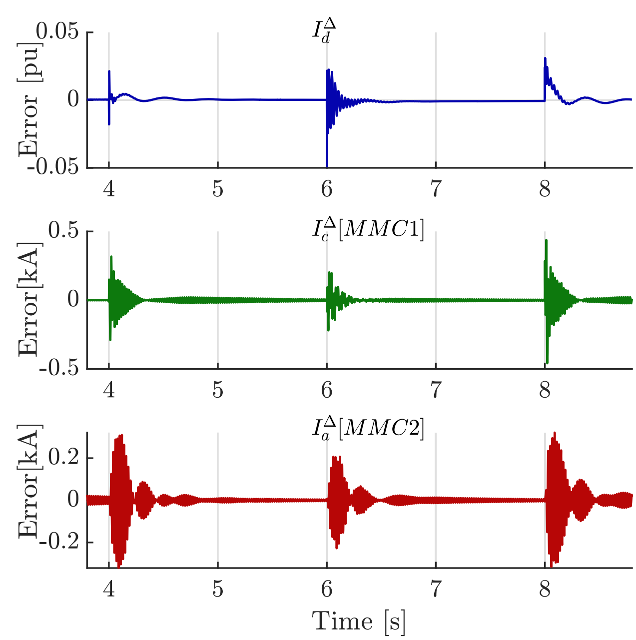

Fig. 10. *DQsym* versus EMT current error comparison: I^{Δ}_{d}, I^{Δ}_{c}(MMC1), and I^{Δ}_{a}(MMC2).

inductance and turn ratio of the connecting transformer, while R_f and L_f are the equivalent resistance and inductance of the filter. Furthermore, the three-phase circulating current dynamics in the stationary frame can be written as

$$L_{arm}\frac{d\vec{i}_j^{\Sigma}}{dt} = \frac{v_{dc}}{2}\vec{1} - R_{arm}\vec{i}_j^{\Sigma} - \vec{v}_{mj}^{\Sigma}, \tag{21}$$

where v_{dc} is the dc-link voltage, $\vec{1} \triangleq [1\ 1\ 1]^T$, and $\vec{v}_{mj}^{\Sigma}$ is the modulated voltage driving the circulating current defined as $\vec{v}_{mj}^{\Sigma} \triangleq [v_{ma}^{\Sigma}\ v_{mb}^{\Sigma}\ v_{mc}^{\Sigma}]^T$. These signals can be expressed as

$$\vec{v}_{mj}^{\Sigma} \triangleq \frac{1}{2}\left(\vec{m}_j^{\Delta} \odot \vec{v}_{C,j}^{\Delta} + \vec{m}_j^{\Sigma} \odot \vec{v}_{C,j}^{\Sigma}\right). \tag{22}$$

Similarly, the dynamics of the voltage sum and difference between the equivalent capacitors of the average model can be expressed, respectively, as

$$\begin{aligned} 2C_{arm}\frac{d\,\vec{v}_{C,j}^{\Sigma}}{dt} &= \vec{m}_j^{\Delta} \odot \tfrac{1}{2}\vec{i}_j^{\Delta} + \vec{m}_j^{\Sigma} \odot \vec{i}_j^{\Sigma}, \\ 2C_{arm}\frac{d\,\vec{v}_{C,j}^{\Delta}}{dt} &= \vec{m}_j^{\Sigma} \odot \tfrac{1}{2}\vec{i}_j^{\Delta} + \vec{m}_j^{\Delta} \odot \vec{i}_j^{\Sigma}. \end{aligned} \tag{23}$$

4.1. MMC model using DP

Eqs. (16)–(23) define a nonlinear averaged model of the MMC. The MMC differential equation can be rewritten in terms of dynamic phasors, adhering to their properties by replacing the state variables, inputs, and time derivatives with their corresponding DPs as in (24). The state and input vector, $\vec{x}$, $\vec{u}$, are given as in (25), each state and input variable will be in complex form.

$$\begin{aligned}
&L_{eq}^{ac}\frac{d}{dt}\langle i_j^{\Delta}\rangle_k = \langle v_{mj}^{d}\rangle_k - \langle v_j^{g}\rangle_k - \left(R_{eq}^{ac} + jk\omega_0 L_{eq}^{ac}\right)\langle i_j^{\Delta}\rangle_k \\
&L_{arm}\frac{d}{dt}\langle i_j^{\Sigma}\rangle_k = \frac{v_{dc}}{2} - \langle v_{mj}^{\Sigma}\rangle_k - \left(R_{arm} + jk\omega_0 L_{arm}\right)\langle i_j^{\Sigma}\rangle_k \\
&2C_{arm}\frac{d}{dt}\langle v_{C,j}^{\Sigma}\rangle_k = \frac{1}{2}\sum_{l=-\infty}^{\infty}\langle m_j^{\Delta}\rangle_{k-l}\langle i_j^{\Delta}\rangle_l \\
&\quad + \sum_{l=-\infty}^{\infty}\langle m_j^{\Sigma}\rangle_{k-l}\langle i_j^{\Sigma}\rangle_l - 2C_{arm}\,jk\omega_g\langle v_{C,j}^{\Sigma}\rangle_k \\
&2C_{arm}\frac{d}{dt}\langle v_{C,j}^{\Delta}\rangle_k = \frac{1}{2}\sum_{l=-\infty}^{\infty}\langle m_j^{\Sigma}\rangle_{k-l}\langle i_j^{\Delta}\rangle_l \\
&\quad + \sum_{l=-\infty}^{\infty}\langle m_j^{\Delta}\rangle_{k-l}\langle i_j^{\Sigma}\rangle_l - 2C_{arm}\,jk\omega_g\langle v_{C,j}^{\Delta}\rangle_k \\
&\langle v_{mj}^{\Sigma}\rangle_k = \frac{1}{2}\left(\sum_{l=-\infty}^{\infty}\langle m_j^{\Sigma}\rangle_{k-l}\langle v_{C,j}^{\Sigma}\rangle_l + \sum_{l=-\infty}^{\infty}\langle m_j^{\Delta}\rangle_{k-l}\langle v_{C,j}^{\Delta}\rangle_l\right) \\
&\langle v_{mj}^{\Delta}\rangle_k = \frac{1}{2}\left(\sum_{l=-\infty}^{\infty}\langle m_j^{\Delta}\rangle_{k-l}\langle v_{C,j}^{\Sigma}\rangle_l + \sum_{l=-\infty}^{\infty}\langle m_j^{\Sigma}\rangle_{k-l}\langle v_{C,j}^{\Delta}\rangle_l\right)
\end{aligned} \tag{24}$$

$$\begin{aligned}
\langle\vec{x}_{MMc}\rangle_k &= [\langle\vec{i}_j^{\Delta}\rangle_k \quad \langle\vec{i}_j^{\Sigma}\rangle_k \quad \langle\vec{v}_{C,j}^{\Delta}\rangle_k \quad \langle\vec{v}_{C,j}^{\Sigma}\rangle_k]^T \\
\langle\vec{u}_{MMc}\rangle_k &= [\langle\vec{v}_j^{g}\rangle_k \quad \langle\vec{v}_{m,j}^{\Delta}\rangle_k \quad \langle\vec{v}_{m,j}^{\Sigma}\rangle_k \quad \langle v_{dc,j}\rangle_k]^T
\end{aligned} \tag{25}$$

4.2. MMC DP model in DQsym

A series of transformations must be applied to represent the MMC DP model in $DQsym$. As described earlier in (2), a symmetrical transformation, T_{pnz}, followed by a rotation for the Positive and negative sequence components, T_{Rot}, will result in each sequence component represented using $DQsym$ components. The state and input vector are given as in (26) where $j2 \in \{p, n, z\}$. Each state and input variable will be in complex form, where $\Re$ equals the d component and $\Im$ equals the q component.

$$T_{pnz}^{dq} = T_{Rot}.T_{pnz} \quad \langle\vec{x}\rangle_k^{dq} = T_{pnz}^{dq}\langle\vec{x}\rangle_k \quad \langle\vec{u}\rangle_k^{dq} = T_{pnz}^{dq}\langle\vec{u}\rangle_k$$

$$\begin{aligned}
\langle\vec{x}_{MMc}\rangle_k^{dq} &= [\langle\vec{i}_{j2}^{\Delta}\rangle_k^{dq} \quad \langle\vec{i}_{j2}^{\Sigma}\rangle_k^{dq} \quad \langle\vec{v}_{C,j2}^{\Delta}\rangle_k^{dq} \quad \langle\vec{v}_{C,j2}^{\Sigma}\rangle_k^{dq}]^T \\
\langle\vec{u}_{MMc}\rangle_k^{dq} &= [\langle\vec{v}_{j2}^{g}\rangle_k^{dq} \quad \langle\vec{v}_{m,j2}^{\Delta}\rangle_k^{dq} \quad \langle\vec{v}_{m,j2}^{\Sigma}\rangle_k^{dq} \quad \langle v_{dc,j2}\rangle_k^{dq}]^T
\end{aligned} \tag{26}$$

The same procedure is applied to the second MMC to derive its state-space representation. The overall system matrices are then obtained by interconnecting the two MMC subsystems. The resulting overall system state and input vectors are defined as given in (27).

$$\langle\vec{x}\rangle_k^{dq} = \begin{bmatrix}\langle\vec{x}_{\mathrm{MMC1}}\rangle_k^{dq} \\ \langle\vec{x}_{\mathrm{MMC2}}\rangle_k^{dq}\end{bmatrix} \qquad \langle\vec{u}\rangle_k^{dq} = \begin{bmatrix}\langle\vec{u}_{\mathrm{MMC1}}\rangle_k^{dq} \\ \langle\vec{u}_{\mathrm{MMC2}}\rangle_k^{dq}\end{bmatrix} \tag{27}$$

Table 1
Test case data.

Parameter & Description	Value
R_s: AC system resistance	892 mΩ
L_s: AC system inductance	16.8 mH
S_b: MMC Base power	1000 MVA
R_{arm}: MMC Arm resistance	166 mΩ
R_t: Equivalent transformer resistance	400 mΩ
R_L: Equivalent load resistance	240 Ω
L_{arm}: MMC Arm inductance	52.94 mH
L_t: Equivalent transformer inductance	52 mH
C: Submodule capacitance	1.758 mF
N: Number of submodules	216
ω_g: Fundamental grid frequency	$2\pi \cdot 50$ rad/s
V_{DC}: Rated pole-to-pole DC voltage	640 kV
V_{PCC}: Rated line-to-line PCC voltage	400 kV
V_{sec}: Rated transformer secondary voltage, line-to-line	333 kV
$K_p^{i,out}$: Output current controller proportional gain	0.6 A/V
$K_i^{i,out}$: Output current controller integral gain	6 A/(V·s)
K_p^{Q}: Reactive power controller proportional gain	0.167 A/V
K_i^{Q}: Reactive power controller integral gain	1 A/(V·s)
$K_p^{i,z}$: Zero-sequence circulating current controller proportional gain	1 A/V
$K_i^{i,z}$: Zero-sequence circulating current controller integral gain	5 A/(V·s)

5. Validation

The simulated point-to-point HVDC power system is depicted in Fig. 4 with MMC parameters of both converters and AC system parameters, both given in Table 1.

The test case begins with the pre-charging session of MMC1 through a pre-insertion resistor, which limits the inrush charging current of the submodule capacitors. During this stage, the capacitor voltages gradually increase until they reach their nominal level. At $t = 0.05$ s, the pre-charging stage is completed, and the start-up resistor is bypassed by closing a Breaker, thereby transitioning the converter into normal operation.

Fig. 5 compares the DC-link voltage responses obtained from EMT and $DQsym$. The two models show very similar behaviour during energisation and load disturbances. Before the power change at $t = 4$ s, the voltage error is small. During the step, the deviation reaches a maximum of about 2 kV and then quickly decreases, returning to a small value (around a few volts) by $t \approx 5$ s. This confirms that $DQsym$ captures both the overall DC voltage dynamics and the short transient variations.

Figs. 6 and 7 compare the output voltages and currents of the inverter- and rectifier-side MMCs. The waveforms from $DQsym$ closely match the EMT results. The maximum phase voltage is approximately 3.693×10^5 V. Before the step change, the voltage error is about 200 V (approximately 0.054%). During the step, it increases to about 2 kV (approximately 0.54%), and then settles around 500 V (approximately 0.14%).

For the currents, using $I_{\mathrm{base}} \approx 1.44$ kA (1000 MVA, 400 kV), the pre-step error is about 2 A (0.14%). During the transient, the deviation reaches approximately 200 A (13.9%) and then decreases to around 10 A (0.69%) once the system settles. Similar behaviour is observed on both inverter and rectifier sides, and across phases.

Figs. 8 and 9 further validate the control performance under step changes in the reference signals. The dq-frame variables (V_d and I_d) from EMT and $DQsym$ show nearly identical responses, with errors on the order of 10^{-3}.

Finally, Fig. 10 summarises the current errors during transient events. The results confirm that $DQsym$ reproduces both steady-state and dynamic behaviour with good accuracy, while remaining compatible with the existing control structure. This makes the model suitable for stability studies and time-domain simulations.

6. Conclusion

This paper presented an equivalent modular multilevel converter (MMC) model formulated within the generalized $DQsym$ dynamic phasor framework and implemented in a numerically stable state-space solver. By systematically incorporating harmonic couplings and switching events, the proposed approach achieves electromagnetic transient (EMT)-level fidelity while operating within a phasor-domain formulation. Validation on a point-to-point HVDC system confirmed the model's accuracy in capturing both slow energy dynamics and fast transient responses, with close agreement to EMT simulations. The solver's compatibility with standard control structures further enables eigenvalue-based small-signal studies and positions the method as a scalable tool for analyzing converter-dominated grids. Future work will extend the framework to multi-terminal HVDC networks and explore its integration into stability analysis.

CRediT authorship contribution statement

Saif Alsarayreh: Writing – review & editing, Writing – original draft, Visualization, Validation, Methodology, Investigation, Formal analysis, Conceptualization; **Robert Dimitrovski:** Writing – review & editing, Validation, Supervision, Methodology, Funding acquisition, Conceptualization; **Aleksandra Lekić:** Writing – review & editing, Validation, Supervision, Project administration, Funding acquisition, Conceptualization.

Declaration of competing interest

The authors declare that they have no known competing financial interests or personal relationships that could have appeared to influence the work reported in this paper.

Acknowledgment

This work was funded by the CRESYM project Harmony (https://cresym.eu/harmony/)

Data availability

No data was used for the research described in the article.

References

[1] O.C. Sakinci, J. Beerten, Modeling of the modular multilevel converter using dynamic phasors: reduced-order models for small-signal stability analysis, (2022), 2022-01-27.

[2] O.C. Sakinci, A. Lekić, J. Beerten, Generalized impedance-based AC/DC power system modeling for harmonic stability analysis, Int. J. Electr. Power Energy Syst. 143 (2022) 108456. https://doi.org/10.1016/j.ijepes.2022.108456

[3] H. Fang, H. Xiang, S. Li, Y. Xin, J. Zhou, Y. Wang, Dynamic phasor modeling of MMC-HVDC systems, in: 2022 IEEE 5th International Conference on Information Systems and Computer Aided Education (ICISCAE), 2022, pp. 988–995. https://doi.org/10.1109/ICISCAE55891.2022.9927689

[4] C.M. Freitas, E.H. Watanabe, L.F.C. Monteiro, D-q small-signal model for grid-Forming MMC and its application in electromagnetic-transient simulations, Energies 16 (5) (2023). https://doi.org/10.3390/en16052195

[5] J.D. Lara, R. Henriquez-Auba, D. Ramasubramanian, S. Dhople, D.S. Callaway, S. Sanders, Revisiting power systems time-domain simulation methods and models, IEEE Trans. Power Syst. 39 (2) (2024) 2421–2437. https://doi.org/10.1109/TPWRS.2023.3303291

[6] J.K.M. Becker, A.M. Kettner, Y. Zuo, F. Cecati, S. Pugliese, M. Liserre, M. Paolone, Modelling of AC/DC interactions of converter-Interfaced resources for harmonic power-flow studies in microgrids, IEEE Trans. Smart Grid 14 (3) (2023) 2096–2110. https://doi.org/10.1109/TSG.2022.3216910

[7] C. Shah, J.D. Vasquez-Plaza, D.D. Campo-Ossa, J.F. Patarroyo-Montenegro, N. Guruwacharya, N. Bhujel, R.D. Trevizan, F.A. Rengifo, M. Shirazi, R. Tonkoski, R. Wies, T.M. Hansen, P. Cicilio, Review of dynamic and transient modeling of power electronic converters for converter dominated power systems, IEEE Access 9 (2021) 82094–82117. https://doi.org/10.1109/ACCESS.2021.3086420

[8] J. Dinkelbach, G. Nakti, M. Mirz, A. Monti, Simulation of low inertia power systems based on shifted frequency analysis, Energies 14 (7) (2021). https://doi.org/10.3390/en14071860

[9] H. Holttinen, J. Kiviluoma, D. Flynn, J.C. Smith, A. Orths, P.B. Eriksen, N. Cutululis, L. Söder, M. Korpås, A. Estanqueiro, J. MacDowell, A. Tuohy, T.K. Vrana, M. O'Malley, System impact studies for near 100% renewable energy systems dominated by inverter based variable generation, IEEE Trans. Power Syst. 37 (4) (2022) 3249–3258. https://doi.org/10.1109/TPWRS.2020.3034924

[10] U. Markovic, O. Stanojev, P. Aristidou, E. Vrettos, D. Callaway, G. Hug, Understanding small-signal stability of low-inertia systems, IEEE Trans. Power Syst. 36 (5) (2021) 3997–4017. https://doi.org/10.1109/TPWRS.2021.3061434

[11] M. Mirz, J. Dinkelbach, A. Monti, DPsim—advancements In power electronics modelling using shifted frequency analysis and in real-time simulation capability by parallelization, Energies 13 (15) (2020). https://doi.org/10.3390/en13153879

[12] R. Dimitrovski, S. Alsarayreh, A. Lekić, A novel dynamic phasor-based mathematical framework for hybrid AC/DC power system simulation (2025). https://doi.org/10.36227/techrxiv.175790504.44615616/v1.

[13] L. Beloqui Larumbe, Harmonic Stability and Distortion in Offshore Wind Farms, Dissertation (tu delft), Delft University of Technology, 2024. https://doi.org/10.4233/uuid:2d917deb-1a14-414a-b475-956455d9b4ce

[14] V.N. Sewdien, Sub synchronous oscillations in modern transmission grids: Design and validation of novel concepts for mitigating adverse dfig-ssr interactions, Dissertation (tu delft), Delft University of Technology, 2021. https://doi.org/10.4233/uuid:8b23ce5e-fd8c-4475-972d-bc50d7a2df1a

[15] A.M. Stankovic, S.R. Sanders, T. Aydin, Dynamic phasors in modeling and analysis of unbalanced polyphase AC machines, IEEE Trans. Energy Convers. 17 (1) (2002) 107–113. https://doi.org/10.1109/60.986446

[16] M. Mirz, A dynamic phasor real-time simulation based digital twin for power systems; 1. Auflage, Dissertation, RWTH Aachen University, Aachen, 2020. Auch veröffentlicht auf dem Publikationsserver der RWTH Aachen University; Dissertation, RWTH Aachen University, 2020, https://doi.org/10.18154/RWTH-2020-10412

[17] Y. Cai, J. Zhang, W. Yu, A predictor-corrector method for power system variable step numerical simulation, IEEE Trans. Power Syst. 34 (4) (2019) 3283–3285. https://doi.org/10.1109/TPWRS.2019.2908054

[18] G. Tzounas, G. Hug, Unified numerical stability and accuracy analysis of the partitioned-solution approach, IEEE Trans. Power Syst. 39 (2) (2024) 3141–3152. https://doi.org/10.1109/TPWRS.2023.3292420

[19] G. Bergna-Diaz, J. Freytes, X. Guillaud, S. D'Arco, J.A. Suul, Generalized voltage-based state-Space modeling of modular multilevel converters with constant equilibrium in steady state, IEEE J. Emerg. Sel. Top. Power Electron. 6 (2) (2018) 707–725. https://doi.org/10.1109/JESTPE.2018.2793159

[20] M.M. Belhaouane, M. Ayari, X. Guillaud, N.B. Braiek, Robust control design of MMC-HVDC systems using multivariable optimal guaranteed cost approach, IEEE Trans. Ind. Appl. 55 (3) (2019) 2952–2963. https://doi.org/10.1109/TIA.2019.2900606